Determination of O[H] and CO Coverage and Adsorption Sites on PtRu Electrodes in an Operating PEM Fuel Cell

Christina Roth,*,[†] Nathalie Benker,[†] Thorsten Buhrmester,[†] Marian Mazurek,[†] Matthias Loster,[‡] Hartmut Fuess,[†] Diederik C. Koningsberger,[§] and David E. Ramaker[¶]

Contribution from the Institute for Materials Science, Darmstadt University of Technology Petersenstrasse 23, D-64287, Darmstadt, Germany, Zentrum für Sonnenenergie- und Wasserstoff-Forschung, Helmholtzstrasse 8, D-89081 Ulm, Germany, Department of Inorganic Chemistry and Catalysis, Debye Institute, Utrecht University, P.O. Box 80083, 3508 TB Utrecht, The Netherlands, and Chemistry Department, George Washington University, Washington, DC 20052

Received January 10, 2005; E-mail: c_roth@tu-darmstadt.de

Abstract: A special in situ PEM fuel cell has been developed to allow X-ray absorption measurements during real fuel cell operation. Variations in both the coverage of O[H] (O[H] indicates O and/or OH) and CO (applying a novel $\Delta\mu_{L3} = \mu_{L3}(V) - \mu_{L3}(ref)$ difference technique), as well as in the geometric (EXAFS) and electronic (atomic XAFS) structure of the anode catalyst, are monitored as a function of the current. In hydrogen, the N_{Pt-Ru} coordination number increases much slower than the N_{Pt-Pt} with increasing current, indicating a more reluctant reduction of the surface Pt atoms near the hydrous Ru oxide islands. In methanol, both O[H] and CO adsorption are separately visible with the $\Delta\mu$ technique and reveal a drop in CO and an increase in OH coverage in the range of 65−90 mA/cm². With increasing OH coverage, the Pt−O coordination number and the AXAFS intensity increase. The data allow the direct observation of the preignition and ignition regions for OH formation and CO oxidation, during the methanol fuel cell operation. It can be concluded that both a bifunctional mechanism and an electronic ligand effect are active in CO oxidation from a PtRu surface in a PEM fuel cell.

Introduction

Platinum is the most promising catalyst for the oxidation of hydrogen in a low-temperature proton exchange membrane (PEM) fuel cell. Its superior catalytic activity, however, drops severely with time when traces of carbon monoxide are present in the feedstock. Since for economic reasons it is desirable to substitute pure hydrogen by less-costly alternatives such as methanol, the development of less CO-sensitive catalysts is of vital importance in fuel cell research. Various binary and ternary Pt alloy catalyst systems[1−7] have been tested recently, showing improved activity for the hydrogen oxidation reaction in the presence of CO. An enhanced activity has been observed particularly for the binary Pt−Ru system.[8]

The platinum anode is poisoned by the CO generated either during the methanol oxidation reaction (MOR) or, even at low concentrations (10−100 ppm), in the hydrogen oxidation reaction (HOR). The CO poison is not oxidized away unless the anode potential is increased to greater than 0.6 V (RHE), where OH adsorption allows the CO oxidation via a Langmuir−Hinshelwood type surface reaction between CO_{ad} and OH_{ad}. The net result of this increase in potential is an unacceptable loss of cell voltage and efficiency.[9] The precise reason for the superior performance of binary catalysts is not known. At least three different mechanisms have been proposed, whereby the alloying element[10] (a) modifies the electronic properties of the Pt by contributing d-electron density (the so-called ligand or electronic mechanism) (b) blocks the CO poison formation reaction, or (c) induces electrosorption of oxygen-containing species O[H] at lower potential, which can then take part in the CO oxidation reaction that removes it from the surface (the so-called bifunctional mechanism).

Two different ligand or electronic mechanisms have been proposed: one that indicates that the Ru reduces the strength

[†] Darmstadt University of Technology.
[‡] Zentrum für Sonnenenergie- und Wasserstoff-Forschung.
[§] Utrecht University.
[¶] George Washington University.

(1) Schmidt, T. J.; Noeske, M.; Gasteiger, H. A.; Behm, R. J.; Britz, P.; Bönnemann, H. *J. Electrochem. Soc.* **1998**, *145*, 925.
(2) Schmidt, T. J.; Gasteiger, H. A.; Stäb, G. D.; Urban, P. M.; Kolb, D. M.; Behm, R. J. *J. Electrochem. Soc.* **1999**, *146*, 1296.
(3) Reetz, M. T.; Lopez, M.; Grünert, W.; Vogel, W.; Mahlendorf, F. *J. Phys. Chem. B* **2003**, *107*, 7414
(4) Grgur, B. N.; Markovic, N. M.; Ross, P. N. *J. Electrochem. Soc.* **1999**, *146*, 1613.
(5) Schmidt, T. J.; Gasteiger, H. A.; Behm, R. J. *J. New Mater. Electrochem. Syst.* **1999**, *2*, 27.
(6) Goetz, M.; Wendt, H. *J. Appl. Electrochem.* **2001**, *31* (7), 811.
(7) Roth, C.; Goetz, M.; Fuess, H. *J. Appl. Electrochem.* **2001**, *31* (7), 793.

(8) Gasteiger, H. A.; Markovic, N. M.; Ross, P. N., Jr.; Cairns, E. J. *J. Phys. Chem.* **1994**, *98* (2), 617.
(9) Gasteiger, H. A.; Markovic, N.; Ross, P. N., Jr.; Cairns, E. J. *J. Phys. Chem.* **1993**, *97*, 12020.
(10) Rauhe, B. R., Jr.; McLarnon, F. R.; Cairns, E. J. *J. Electrochem. Soc.* **1995**, *142*, 1073.

of the Pt—CO bond[11] and a second that it lowers the required potential for activation of water to form OH which oxidizes the CO.[12] Although the bifunctional mechanism is preferred by a majority of workers in the field, some in situ experimental results on PtSn, for example, suggest that the electronic mechanism is more active,[13] and both may be active in some cases.[12,14−16]

There exist a multitude of characterization methods that might be applied for in situ investigations to answer these questions, some which directly reveal CO adsorption sites, such as Fourier transform infrared (FTIR)[11,17] and optical sum frequency generation (SHG).[18] X-ray absorption fine structure spectroscopy (XAFS) has proven to be an appropriate technique for this purpose as suggested by the comparatively large number of in situ XAS studies that have been published during the past decade.[19−25] XAFS is highly versatile, since in situ measurements can be carried out in different environments, different atmospheres, and at various temperatures. Thus, a variety of problems in fuel cell research can be addressed, e.g., temperature-dependent structural changes of the catalysts, the effect of different electrode potentials,[22−24] and the impact of H, OH, and CO adsorption[25] on the catalyst structure. Numerous investigations have contributed to the detailed characterization of the catalyst structure before their application in a fuel cell[26−30] (labeled "blank" in this work) or in situ in conventional electrochemical cells in aqueous electrolyte[21,22] under fuel cell-relevant conditions. However, to our knowledge only a few reported studies have been carried out under operating conditions (operando) in a working fuel cell.[31,32] Similar information could be obtained perhaps more conveniently in an electrochemical or half-cell; however, significant differences in the environment of the electrode surface can exist in these systems, such as the extent of hydration of the electrode surface, the interface with
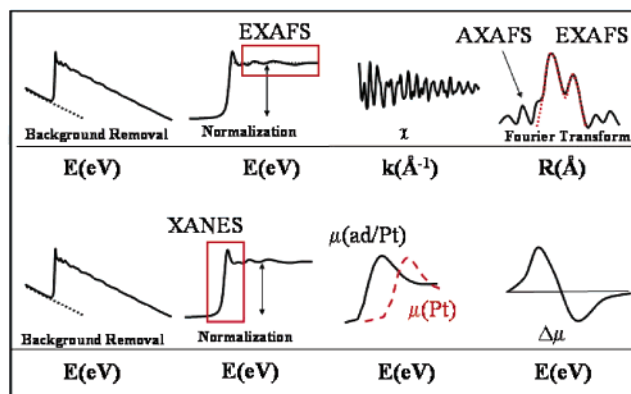
Figure 1. Top: Schematic showing the removal of background and normalization of the raw data, extraction of the EXAFS signal (χ), and finally least-squares fit of model functions to the Fourier transform of χ to obtain the EXAFS parameters given in Tables 1 and 2. Also indicated is the AXAFS signal at low R. Bottom: Schematic showing the removal of background, normalization, and then the difference in the XANES region to give the $\Delta\mu$ spectra.

Nafion, introduction of the H_2 gas via a gas membrane versus through the electrolyte, the acidity of the electrolyte, and other possible variables. The desire to examine a real supported PtRu/C anode in an operating fuel cell motivates these operando studies.

In this study, operando XAFS investigations have been conducted in a specifically modified fuel cell in hydrogen and methanol operation.[32] Both the extended X-ray absorption fine structure (EXAFS) and near-edge structure (XANES) in the X-ray absorption data are utilized as summarized in Figure 1. The Pt L_3-edge data of the PtRu/C electrode were processed using the XDAP code by M. Vaarkamp et al.,[33] which uses a cubic spline background subtraction procedure allowing a continuous adjustable smooth parameter. Therefore, this software has a significant advantage in that it enables the evaluation of the so-called "atomic" X-ray absorption fine structure (AXAFS) visible in the Fourier transform as shown in Figure 1. This comparatively new AXAFS approach provides *electronic* in addition to the conventional EXAFS *geometric* information. In addition, a new $\Delta\mu$ XANES analysis procedure[26,34,35] illustrated in Figure 1 supplies information about adsorbate coverage and even specific adsorption sites on the Pt. Consequently, changes in adsorbate coverage and in the catalyst structure due to, e.g., electrochemical potential[23] and interaction with the support material, can be observed, making these novel approaches extremely suitable for the investigation of catalysts as a function of the fuel cell current or potential. As a result of these techniques, detailed changes in the PtRu structure, incipient oxide coverage, electrode charging, and in both the O[H] and CO coverage and adsorption sites on Pt have been monitored as a function of the fuel cell current. Although CO coverage has been monitored previously with spectroscopic techniques,[11,17,18] this is the first study of the current dependence of the OH coverage in H_2 and methanol in a working fuel cell that we are aware of.

(11) Brankovic, S. R.; Marinkovic, N. S.; Wang, J. X.; Adžić, R. R. *J. Electroanal. Chem.* **2002**, *532*, 57.
(12) Lu, C.; Rice, C.; Masel, R. I.; Babu, P. L.; Waszczuk, P.; Kim, H. S.; Oldfield, E.; Wieckowski, A. *J. Phys. Chem. B* **2002**, *106*, 9581.
(13) Gasteiger, H. A.; Markovic, N. M.; Ross, P. N., Jr. *J. Phys. Chem.* **1995**, *99*, 8945.
(14) Samjeske, G.; Xiao, X. Y.; Baltrushat, H. *Langmuir* **2002**, *18*, 4659.
(15) Kei, H. W.; Suh, S.; Gurau, B.; Workie, B.; Liu, R. X.; Smotkin, E. S. *Electrochim. Acta* **2002**, *47*, 2913.
(16) Lu, G. Q.; Waszczuk, P.; Wieckowski, A. *J. Electroanal. Chem.* **2002**, *532*, 49.
(17) Xia, X. H.; Iwasita, T.; Ge, F.; Vielstich, W. *Electrochim. Acta* **1996**, *41*, 711.
(18) Lu, G.-Q.; White, J. O.; Wieckowski, A. *Surf. Sci.* **2004**, *564*, 131.
(19) McBreen, J. In *Physical Electrochemistry: Principles, Methods and Applications*; Rubinstein, I., Ed.; Marcel Dekker: New York, Basel, Hongkong, 1995; p 339.
(20) McBreen, J.; Mukerjee, S. In *Interfacial Electrochemistry*; Wieckowski, A., Ed.; Marcel Dekker: New York, 1998; p 895.
(21) Lampitt, R. A.; Carrette, L. P. L.; Hogarth, M. P.; Russell, A. E. *J. Electroanal. Chem.* **1999**, *460*, 80.
(22) Mukerjee, S.; Urian, R. C. *Electrochim. Acta* **2002**, *47*, 3219.
(23) O'Grady, W. E.; Ramaker, D. E.; Qian, X. *J. Phys. Chem. B* **1997**, *101*, 5624; O'Grady, W. E.; Ramaker, D. E. *Electrochim. Acta* **1998**, *44*, 1283.
(24) O'Grady, W. E.; Hagans, P. L.; Pandya, K. I.; Maricle, D. L. *Langmuir* **2001**, *17*, 3047.
(25) Maniguet, S.; Mathew, R. J.; Russell, A. E. *J. Phys. Chem. B* **2000**, *104*, 1998−2000.
(26) Teliska, M.; O'Grady, W. E.; Ramaker, D. E. *J. Phys. Chem. B* **2004**, *108*, 2333.
(27) Liu, Z.; Lee, J. Y.; Han, M.; Chen, W.; Gan, L. M. *J. Mater. Chem.* **2002**, *12*, 2453.
(28) Rolinson, D. R.; Hagans, P. L.; Swider, K. E.; Long, J. W. *Langmuir* **1999**, *15*, 774−779.
(29) Lasch, K.; Jörissen, L.; Garche, J. *J. Power Sources* **1999**, *84*, 225.
(30) Roth, C.; Martz, N.; Fuess, H. *J. Phys. Chem. Phys.* **2001**, *3*, 315.
(31) Viswanathan, R.; Hou, G.; Liu, R.; Bare, S. R.; Modica, F.; Mickelson, G.; Segre, C. U.; Leyarovska, N.; Smotkin, E. S. *J. Phys. Chem. B* **2002**, *106*, 3458.
(32) Roth, C.; Martz, N.; Buhrmester, Th.; Fuess, H. *Phys. Chem. Chem. Phys.* **2002**, *4*, 3555.

(33) http://www.xsi.nl, XDAP software, code and licensing, last updated August 2005, last accessed September 2005.
(34) Ramaker, D. E.; Koningsberger, D. C. *Phys. Rev. Lett.* **2002**, *89*, 701.
(35) Teliska, M.; O'Grady, W. E.; Ramaker, D. E. *J. Phys. Chem. B* **2005**, *109*, 8076−8084.

Experimental and Methods Section

MEA Preparation. Several membrane-electrode assemblies (MEAs) were prepared by a spraying technique originally developed by Wilson and Gottesfeld.[36] Pt (20 wt % on Vulcan XC 72) served as the catalysts at the cathode and a Pt–Ru (1:1, 20 wt % on Vulcan XC 72) alloy as the anode catalyst, both commercially available from E-TEK Inc. In contrast to our standard single-cell measurements, the platinum loading of each membrane-electrode assembly was increased up to at least 1.2 mg/cm^2 per electrode providing the best compromise between a calculated optimum signal-to-noise ratio (XAS) and almost unchanged electrode features with respect to current distribution and transport processes. The catalysts were mixed with Nafion ionomer and water to form an ink, homogenized in an ultrasonic bath, and sprayed in successive layers onto a commercial Nafion 117 ion exchange membrane from DuPont. All MEAs were prepared at ZSW in Ulm, Germany, left to dry, and then stored in a sealed box. Measurements were carried out on two different membrane-electrode assemblies in both hydrogen and methanol operation to check the reproducibility of the data.

In Situ Fuel Cell Setup. A commercially available graphite cell hardware (Electrochem. Inc.) was modified to allow for beam penetration perpendicular to the membrane-electrode assembly. Small channels were cut into the graphite flow fields of both half-cells (for details see ref 32). As absorption in graphite is negligible in the respective energy range (11564 eV at the Pt L$_3$-edge), it served as an inherent beam window. A graphite window thickness of 0.4 mm proved to be thick enough to tighten the cell completely and separate hydrogen from oxygen. Holes of 1.5 cm × 0.7 cm were drilled into the bipolar plates to let the beam pass unhindered. For this reason, the position of the heating pads was changed slightly. The applicability of the thus modified cell was tested without gas flow at elevated temperatures initially ("blank" measurements). However, in the chosen setup, both electrodes were monitored simultaneously, i.e., changes at the anode side could not be separated from those at the cathode. Hence, a 10 mm × 2 mm area of the cathode had to be removed in the respective window region in order to obtain exclusively the contribution from the anode side. The main disadvantage of this procedure is that it might modify the current distribution within the membrane-electrode assembly, but as discussed above one could obtain somewhat comparable data without an O anode present at all, so this is not expected to modify our results significantly. To overcome this possible problem completely, in other work experiments have been carried out in fluorescence geometry,[37] since in this setup neither the removal of part of the cathode nor an increase in catalyst loading are required.

Fuel Cell XAFS Measurements. Prior to the measurements, the fuel cell was heated to the correct working temperature and purged with nitrogen for a couple of minutes to free the hydrogen pipe from air. The feed gases were supplied by commercially available mass flow controllers (Bronkhorst). In hydrogen operation, 150 mL/min of H$_2$ (N 5.0, Linde) was loaded with water in a humidifier ($T = 70$ °C) and fed into the fuel cell anode. As cathode feed, high-purity oxygen was supplied (N 4.5, Linde) at 75 mL/min. In methanol mode, 1 mL/min of a 1 M aqueous methanol solution (Aldrich) was fed into a vaporizer by a peristaltic pump and evaporated at $T = 130$ °C. The fuel cell supply with the methanol vapor was realized by a supporting nitrogen gas flow (50 mL/min) via a curing tube. An amount of 100 mL/min oxygen served as cathode feed in direct methanol operation. In contrast to the H$_2$ measurement, in methanol mode the cell was heated to $T = 95$ °C and held at this temperature during operation. E/i curves were recorded galvanostatically, using an electronic load and a potentiometer both manufactured in-house. Typical current–voltage characteristics recorded in hydrogen and methanol operation in this setup can be found

in ref 28. The values obtained during these experiments are below standard, presumably due to the increased electrode thickness and the removal of part of the cathode in the beam window region. Various spectra were recorded at the Pt L$_3$-edge at several points along the curve in the activation, resistivity, and diffusion regime. A holding time of approximately 20 min at each current value was applied, after which a quasi-steady-state had been reached. Blank experiments for each MEA in its dry state were carried out at elevated temperatures but in absence of gases to serve as reference.

XAFS Data Collection. All XAFS data were collected at beamline X1 of Hasylab, Hamburg. This beamline offers an energy range of 6–80 keV and a resolution of approximately 1 eV at the Pt L$_3$-edge. The synchrotron source was operated at an energy of 4.45 GeV and an initial positron beam current of 120 mA. All XAS spectra were recorded in transmission geometry from $E = 11\,550$ up to 12 900 eV (Pt L$_3$-edge at 11 564 eV), using a thin Pt metal foil as reference. A Si(111) monochromator was applied and detuned to 50% intensity to minimize the presence of higher harmonics. The intensities of the focused beam and the transmitted beam were detected by three gas-filled ion chambers in series. Analysis of the data was carried out by the program package XDAP developed by Vaarkamp et al.[33,38] Details of this EXAFS analysis are given in the Supporting Information.

Analysis of the Pt L$_3$ X-ray Absorption Spectra. As summarized in Figure 1, the preedge was approximated by a modified Victoreen curve. The energy scale was calibrated by the second derivative of the Pt-foil spectrum, and the edge position was determined as the first inflection point. Normalization was carried out by dividing the data by the height of the absorption 50 eV above the absorption edge. The background was subtracted employing cubic spline routines with a continuously adjustable smooth parameter.[39] This made it possible to generate the normalized oscillatory part of the XAFS data (the EXAFS), as well as the AXAFS contribution. The EXAFS data analysis program XDAP allows one to perform multiple-shell fitting in R-space by minimizing the residuals between both the absolute and the imaginary part of the Fourier transforms of the data and a model containing parameters for the Pt average coordination number, N, the average Pt–Pt and Pt–O nearest neighbor distances, R, a Debye–Waller factor ($\Delta\sigma^2$) to account for static and dynamic disorder, and a standard reference shift parameter, E_0. Full details of this analysis can be found in the Supporting Information.

It is well-known that the Pt L$_3$ XANES is sensitive to the adsorption of various adsorbates. To isolate and identify the rather small changes that arise due to adsorbates, difference spectra $\Delta\mu$ are obtained by taking the difference between the L$_3$ spectra with and without the adsorbate (denoted in the following by Ad), $\Delta\mu = \mu(\text{Ad/Pt}) - \mu(\text{Pt})$, following a procedure reported previously[26,34,35,41] and illustrated in Figure 1. Here, $\mu(\text{Ad/Pt})$ is the L$_3$-edge spectrum in the presence of Ad and $\mu(\text{Pt})$ the L$_3$-edge spectrum at some different potential or current where the adsorbate coverage is known to be generally much smaller, or at least very different, so that the effect of the adsorbate can be isolated.

The FEFF8 code[40] was designed to calculate μ just as that obtained in the experiment. FEFF8 performs real-space full multiple-scattering calculations utilizing a muffin-tin potential calculated with Hedin–Lundquist exchange correlation approximation and implements self-consistent field potentials for the determination of the Fermi level and the charge transfer. A core-hole is included on the absorber atom in order to mimic the final state of the photon absorption process. Thus $\Delta\mu$ can be calculated by performing the same $\Delta\mu$ difference as obtained experimentally; i.e., $\Delta\mu = \mu(\text{Ad/Pt}_6) - \mu(\text{Pt}_6)$ where Pt$_6$ denotes a cluster of 6 Pt atoms as shown in Figure 2.

(36) Wilson, M. S.; Gottesfeld, S. *J. Appl. Electrochem.* **1992**, *22*, 1.
(37) Roth, C.; Martz, N.; Mazurek, M.; Scheiba, F.; Fuess, H. *Adv. Eng. Mater.* **2005**, in press.
(38) Vaarkamp, M.; Linders, J. C.; Koningsberger, D. C. *Physica B* **1995**, *208/209*, 159.
(39) van Dorssen, G. E.; Koningsberger, D. C.; Ramaker, D. E. *J. Phys.: Condens. Matter* **2002**, *14*, 13529.
(40) Ankudinov, A. L.; Ravel, B.; Rehr, J. J.; Conradson, S. D. *Phys. Rev. B* **1998**, *58*, 7565.
(41) Ramaker, D. E.; Teliska, M.; Zhang, Y.; Stakheev, A. Yu.; Koningsberger, D. C. *Phys. Chem. Chem. Phys.* **2003**, *5*, 4492.
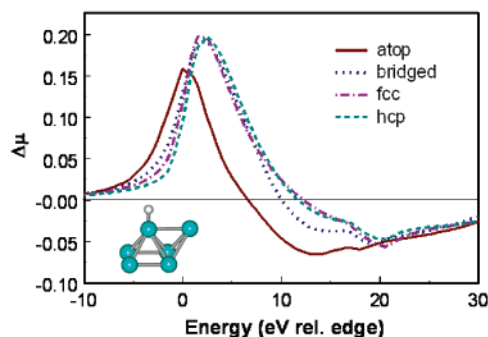
Figure 2. $\Delta\mu = \mu(O/Pt_6) - \mu(Pt_6)$ signatures for atop, bridge, fcc, and hcp adsorbed O on Pt as obtained from FEFF8 calculations on the Pt_6 cluster illustrated. The cluster as shown illustrates an O atom in an atop position.

The theoretical results in Figure 2 show the importance of changes in the Pt L_3 XANES region due to the influence of chemisorbed O on the Pt–Pt multiple scattering paths. When, for example, O[H] (O or OH) species are adsorbed in the atop sites versus the *n*-fold (bridged, fcc, or hcp) sites, both the Pt–Pt scattering and Pt–O scattering change in a different way making the total sensitive to the adsorption site. The theoretically obtained fingerprints for atop and *n*-fold O have been shown previously[35,41] and are given again in Figure 2. Unfortunately, only atop sites can be distinguished from *n*-fold sites, but this is sufficient to distinguish atop OH from *n*-fold O,[35] which is critical in this work. Further, it has been shown previously that if OH is bound to a Pt near another metal atom such as Ni, Co, or Ru, it is shifted downward in energy compared to OH adsorbed at a normal Pt site.[42] Thus, the $\Delta\mu$ XANES not only gives a measure of the coverage but also indicates the binding site, atop OH or *n*-fold O. Moreover, in the case of atop OH, it even indicates if the Pt site has another atom (e.g., Ru) as a neighbor instead of all Pt neighbors.

Results

The final results of the EXAFS data-analysis are given in Tables 1 and 2, for electrode I in H_2 and electrode II in methanol, respectively (the details of this analysis are given in the Supporting Information). Differences are observed in the EXAFS coordination parameters obtained for electrode I and II. The magnitude of the FT AXAFS (illustrated in Figure 1) is also given in Tables 1 and 2. It can be seen that the FT AXAFS amplitude decreases after contact with methanol fuel at 0 mA/cm² and increases again at a current of 88 mA/cm².

Figures 3 and 4 show the differences, $\Delta\mu = \mu(I) - \mu(ref)$, plotted with the highest current density (lowest potential) used as the reference (120 mA/cm² in H_2 and 88 mA/cm² in methanol). Here $\Delta\mu$ has been smoothed with a 3-point smooth lowess functional (3 eV spread total) to reduce the noise level. These $\Delta\mu$ differences show systematic changes at the 1–2% level, with the noise level after smoothing at around 0.2%.

The $\Delta\mu$ data for anode (I) in H_2 in Figure 3, reveal the usual signature for atop and br/fcc O[H], peaking around 3 and 7 eV relative to the edge, respectively, in the experiment, corresponding to peak positions in the theory around 0 and 4 (peaks positions between theory and experiment often disagree by 0–3 eV). However, a third peak at lower energy, around −1 eV, appears. This latter feature is attributed to OH in an atop position on Pt but near a Ru atom. Such a lower energy feature has been

(42) Teliska, M.; Murthi, V. S.; Mukerjee, S.; Ramaker, D. E. In *Proceedings of the Electrochemical Society, 204th Meeting, Fundamental Understanding of Electrode Processes in memory of Professor Ernest B. Yeager*; Prakash, J., Chu, D., Scherson, D., Enayetullah, M., Tae Bae, I., Eds.; The Electrochemical Soc.: Pennington, NJ, 2005, PV 2003-30, p 212.

Table 1. EXAFS Coordination Parameters Obtained by *R*-Space Fit (k^1, $\Delta k = 3-14$ Å⁻¹, $\Delta R = 1.4-3.2$) for Pure Hydrogen Used as Anode Feed[a]

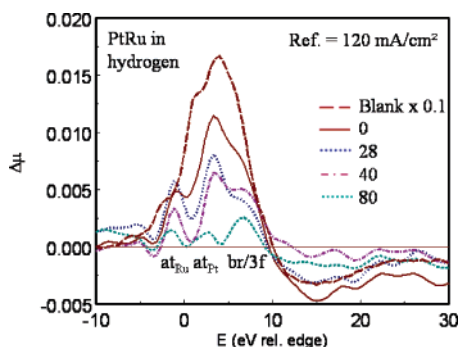| current [mA/cm²]	scatterer	N (± 10%)	R (Å) (± 0.02 Å)	$\Delta\sigma^2$ (Å²) (± 5%)	E_0 (eV) (± 10%)	AXAFS amplitude (× 10⁴)[b]	var im[c]	var abs[d]
blank	Pt	5.7	2.74	0.004	1.8	244	0.4	0.1
	Ru	0.3	2.70	0.002	−3.2			
	O, C	1.6	2.03	0.006	0.7			
0	Pt	7.9	2.73	0.004	1.8	197	0.3	0.1
	Ru	0.6	2.70	0.006	−9.6			
	O, C	0.5	2.02	0.011	−2.2			
28	Pt	8.2	2.75	0.004	2.7	192	0.2	0.1
	Ru	0.7	2.71	0.003	−6.9			
	O, C	0.4	2.02	0.008	−2.4			
40	Pt	8.4	2.75	0.004	2.3	203	0.5	0.2
	Ru	1.0	2.71	0.007	−7.1			
	O, C	0.4	2.02	0.003	−0.7			
80	Pt	8.4	2.75	0.004	1.1	208	0.2	0.1
	Ru	1.0	2.70	0.006	−6.7			
	O, C	0.3	2.02	0.003	−2.5			
120	Pt	8.5	2.75	0.004	1.3	202	0.2	0.1
	Ru	1.2	2.69	0.006	−4.9			
	O, C	0.3	2.02	0.007	−3.7			

[a] The maximum calculated standard deviation is indicated in parentheses. [b] FT AXAFS: k^1, $\Delta k = 3-8$ Å⁻¹. [c] var im: variance of fit of imaginary part of FT. [d] var abs: variance of fit of absolute part of FT.

Table 2. EXAFS Coordination Parameters Obtained by *R*-Space Fit (k^1, $\Delta k = 3-14$ Å⁻¹, $\Delta R = 1.4-3.2$) for Methanol Used as Anode Feed[a]

current [mA/cm²]	scatterer	N (± 10%)	R (Å) (± 0.02 Å)	$\Delta\sigma^2$ (Å²) (± 5%)	E_0 (eV) (± 10%)	AXAFS amplitude (× 10⁴)[b]	var im[c]	var abs[d]
blank	Pt	6.5	2.75	0.004	1.3	250	0.2	0.1
	Ru	0.6	2.70	0.004	−1.9			
	O, C	1.5	2.02	0.005	1.5			
0	Pt	8.2	2.75	0.005	1.8	151	0.3	0.1
	Ru	0.8	2.74	0.007	−7.1			
	O, C	0.7	2.02	0.012	−5.5			
24	Pt	8.2	2.75	0.005	1.5	176	0.2	0.1
	Ru	1.1	2.71	0.007	−7.8			
	O, C	0.5	2.02	0.012	−3.7			
48	Pt	8.4	2.75	0.005	2.6	178	0.3	0.1
	Ru	1.5	2.70	0.011	−6.2			
	O, C	0.3	2.02	0.008	−3.4			
68	Pt	8.0	2.75	0.004	2.3	192	0.3	0.1
	Ru	1.1	2.70	0.007	−6.7			
	O, C	0.5	2.02	0.012	−4.4			
88	Pt	7.7	2.74	0.004	2.3	194	0.4	0.2
	Ru	1.0	2.71	0.006	−8.2			
	O, C	0.5	2.02	0.007	−2.6			

[a] The maximum calculated standard deviation is indicated in parentheses. [b] FT AXAFS: k^1, $\Delta k = 3-8$ Å⁻¹. [c] var im: variance of fit of imaginary part of FT. [d] var abs: variance of fit of absolute part of FT.
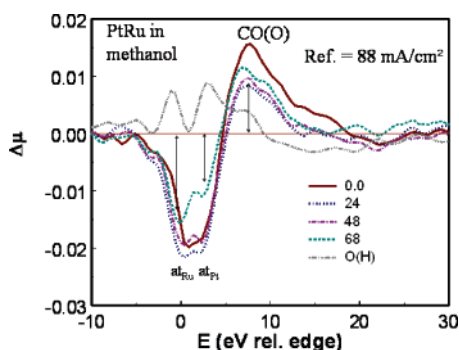
seen before in PtCo and PtNi alloys, while it is absent in pure Pt.[42] That this peak is indeed an OH/Pt near a Ru atom (denoted OH/PtRu here) will be further confirmed using the EXAFS results in the Discussion. This shift to lower energy may result either from an electronic effect of the Ru on the Pt or from lateral interactions between the OH/Ru and the OH/Pt as discussed previously.[42]

Figure 4 compares the $\Delta\mu$ for anode II in methanol (presence of CO), with the $\Delta\mu$ in H_2 at 40 mA/cm². The $\Delta\mu$ signatures in methanol are significantly different in spectral shape from those in H_2 due to the presence of CO poison on the surface in methanol. Methanol-derived surface CO on fuel cell grade Pt

Figure 3. $\Delta\mu = \mu(I) - \mu(120 \text{ mA/cm}^2)$ obtained from the data of anode (I) in H$_2$ (see Figure 5a). The features attributed to atop OH/Pt near a RuO-(H)$_n$ island (denoted as at$_{Ru}$), atop OH/Pt away from a RuO(H)$_n$ island (denoted as at$_{Pt}$), and O in a bridged or fcc position on Pt (denoted as br/3f) are indicated.

Figure 4. $\Delta\mu = \mu(I) - \mu(88 \text{ mA/cm}^2)$ obtained from the data of anode (II) in methanol (see Figure 5b). The features arising from CO/Pt (adsorbed CO) and the negative-going features due to atop OH/Pt (denoted as in Figure 3) are indicated by the vertical lines.

and PtRu alloys has been seen previously with a radioactive labeling technique,[43] as well as spectroscopically on model catalysts.[44] Although other methanol decomposition pathways on a Pt electrode are known, these pathways produce products that dissolve or leave the surface[45] so that CO is the only additional stable adsorbate expected on the surface in methanol. Intermediates in the oxidation of methanol are not expected to live long enough to make them visible in the XANES. Finally FEFF8 calculations for CO/Pt in an atop position (not shown here) confirm that this 8 eV feature arises from CO on the surface,[46] and we use the intensity of this feature to reflect CO on Pt. Unfortunately, the O/Pt feature around 7−8 eV, seen in H$_2$ is masked by the presence of the CO feature.

Discussion

Particle Morphology. The EXAFS results allow considerable insight into the PtRu particle morphology. First the sum of the coordination numbers N_{PtPt} (ca. 8.4) + N_{PtRu} (ca. 1.0) resulting in around 9 indicates particle sizes typical of that for the ETEK samples utilized in fuel cells.[47] Model calculations assuming spherical clusters with fcc packing[48,49] allow us to estimate the

particle diameter to be approximately 2.0−2.5 nm containing around 200−400 metal atoms, with a dispersion (N_{surf}/N_{bulk}) of around 0.4−0.6. This relatively small dispersion only reduces the magnitude of the $\Delta\mu$, since contributions from the Pt atoms in the interior of the cluster do not change appreciably with potential and therefore cancel out (i.e., $\Delta\mu$ reflects conditions at the surface). The small $\Delta\mu$ is not a problem here even with the small (0.1−2%) differences evident in Figures 3 and 4, since the noise level is much smaller. Although adsorption of O could change the shape of these Pt clusters, thereby changing the Pt−Pt EXAFS scattering, such changes should appear above the $\Delta\mu$ range of interest (i.e., above 40 eV) where the Pt−Pt scattering is larger. Thus this work reveals that detailed in situ adsorption information can be obtained even from relatively large PtRu clusters.

The Pt−Pt and Pt−Ru distances give further information about the nature of the bulk alloy. Antolini[47] has recently reviewed the literature involving both bulk PtRu alloys and supported PtRu particles. He points out that for Ru fractions up to about 0.7, Pt and Ru form a solid solution with Ru atoms replacing Pt atoms in the fcc structure. The lattice constant decreases from 3.923 Å (pure Pt) to 3.83 Å at 0.675 atomic fraction Ru.[47] The Pt−Pt distance found in Tables 1 and 2 of 2.75 Å is however not much smaller than that for pure Pt/C particles at 2.75−2.76 Å and is entirely consistent with the value of 2.75 Å found for Pt/Ru 1:1 catalysts on C at 20% loading reported previously.[47] From these data it is generally concluded that only part of the Ru is alloyed with Pt. This partial alloy formation is also consistent with the Pt−Ru/Pt−Pt coordination ratio of 1/8 or less. This ratio is even smaller than that expected for Ru atomic fractions of 0.25−0.33 found by others.[47] The remaining Ru is believed to exist on the surface of the Pt particles as hydrous ruthenium oxide at some unknown oxidation level;[50−53] here denoted as RuO(H)$_n$. The Debye−Waller parameter σ^2 gives some measure of the dynamic and static disorder, but at 0.005−0.007 remains much as it does for pure Pt/C. Thus, the EXAFS data reported here is completely consistent with that reported previously for PtRu/C used in an electrochemical or fuel cell and with conclusions drawn previously about the very inhomogeneous distribution of Ru in the catalysts particles.[47]

Reduction of Pt and RuO(H)$_n$ Islands with Current. In methanol, an increasing amount of O[H] is generally forming on the surface with increasing current, while the amount of CO on the surface is decreasing. Because the μ spectrum at largest current (88 mA/cm^2) in methanol was used as a reference in the $\Delta\mu = \mu(I) - \mu(88)$ difference, features from OH/PtRu and OH/PtPt (labeled at$_{Ru}$ and at$_{Pt}$ in Figure 4 for atop OH adsorption for brevity) are clearly visible as shown by the arrows in Figure 4, but they appear with negative amplitude, while a positive CO(O) feature appears at higher energy. The $\Delta\mu$ amplitudes of these features are plotted in Figure 5a versus current. Of course

(43) Waszczuk, P.; Wieckowski, A.; Zelenay, P.; Gottesfeld, S.; Coutanceau, C.; Léger, J.-M.; Lamy, C. *J. Electroanal. Chem.* **2001**, *511*, 55.
(44) Tong, Y.; Kim, H. S.; Babu, P. K.; Waszczuk, P.; Wieckowski, A.; Oldfield, E. *J. Am. Chem. Soc.* **2002**, *124*, 468.
(45) Lu, G.-Q.; Chrzanowski, W.; Wieckowski, A. *J. Phys. Chem. B* **2000**, *104*, 5566.
(46) Scott, F.; Mukerjee, S.; Ramaker, D. E. submitted 2005.
(47) Antolini, J. *Mater. Chem. Phys.* **2003**, *78*, 563.
(48) de Graaf, J. Ph.D. Dissertation, Utrecht University, Ridderkerk, The Netherlands, 2001.
(49) de Graaf, J.; van Dillen, A. J.; de Jong, K. P.; Koningsberger, D. C. *J. Catal.* **2001**, *203*, 307.
(50) Rolison, D. R.; Hagans, P. L.; Swider, K. E.; Long, J. W. *Langmuir* **1999**, *15*, 774; Stroud, R. A.; Long, J. W.; Swider-Lyons, K. E.; Rolison, D. R. *Microsc. Microanal.* **2002**, *8*, 50.
(51) Viswanathan, R.; Hou, G. Y.; Liu, R. X.; Bare, S. R.; Modica, F.; Mickelson, G.; Segre, C. U.; Leyarovska, N.; Smotkin, E. S. *J. Phys. Chem. B* **2002**, *106*, 3458.
(52) Vogel, W.; Britz, P.; Boennemann, H.; Rothe, J.; Hormes, J. *J. Phys. Chem. B* **1997**, *101*, 11029.
(53) Brankovic, S. R.; Wang, J. X.; Zhu, Y.; Sabatini, R.; McBreen, J.; Adžić, R. R. *J. Electroanal. Chem.* **2002**, *524−525*, 231.
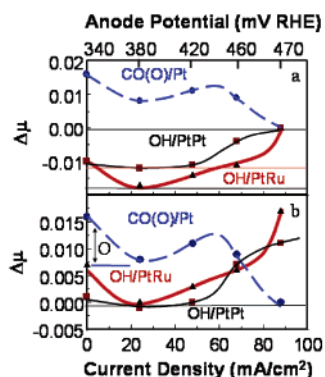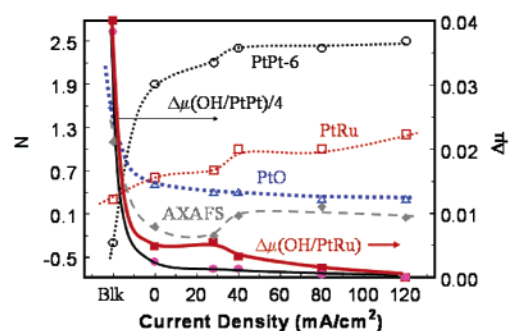
Figure 5. (a) Amplitudes of the three features identified in Figure 4 for methanol as a function of current density (at$_{Pt}$ around −1 eV in Figure 7 now identified as OH/PtPt, at$_{Ru}$ around 3 eV as OH/PtRu, and CO(O) at 7 eV as CO(O)/Pt, see text). The horizontal lines, drawn at the minimum in the OH curves around 24 mA/cm^2, identify the "zero-point" magnitude of $\Delta\mu$ as described in the text. (b) Estimate of adsorbate coverage, after accounting for the "zero-point" difference problem. The horizontal line below 25 mA/cm^2 suggests the CO and O components of the CO(O) coverage. Immediately above 25 mA/cm^2, the O coverage is believed to be negligible, although above 60 mA/cm^2 it may increase again. The numbers at the top indicate the anode potential (V RHE) estimated from Figure 8 as described in the text.

$\Delta\mu$ go to zero for all features at 88 mA/cm^2 because this current was used as the reference.

It is difficult to indicate quantitatively how much CO is still present, if any, or how much O[H] is present on the reference surface at 88 mA/cm^2 in methanol. The $\Delta\mu$ technique by its nature can only indicate the change in coverage, unless one has a "clean" reference. A relatively "clean" reference electrode at 120 mA/cm^2 in H$_2$ is expected assuming near total reduction of the PtRu electrode at this current and that the H$_2$ anode potential stays near zero at some of the lower currents. However in methanol, we can only optimistically presume that the O[H] coverage is very small near the minimum in the O[H] curves around 20−30 mA/cm^2 in Figure 5a. Assumptions are that the electrode has been reduced at this point like in H$_2$ and further that the anode current in methanol remains sufficiently small at this minimum point so that the build up of O[H], which occurs at higher current (higher anode potential), is not yet significant. Further, we assume that the CO coverage is reasonably small at 88 mA/cm^2, which we will show below is beyond the point where significant OH is building up on the surface. Support for relatively low CO coverage at high currents comes from previous kinetic studies.[54] In contrast to that at lower currents when the kinetics is zero order in methanol, these studies have found that at higher currents the kinetics becomes first order in methanol. This suggests that indeed the methanol adsorption is becoming the rate-determining step (RDS) at high currents, in which case the CO coverage should be small with the O[H] coverage large. With these assumptions the OH/PtPt and OH/PtRu $\Delta\mu$ amplitudes in Figure 5a are shifted upward in Figure 5b, with the amount of the upward shift indicated by the "zero-point amplitudes", the horizontal lines in Figure 5a at 0.012 and 0.17, respectively. Figure 5b then reflects the estimated adsorbate coverage in methanol at each current density.

Correlation of the EXAFS, AXAFS, and $\Delta\mu$ results with current in hydrogen (Figure 6) and methanol (Figure 7) reveals

(54) Gurau, B.; Viswanathan, R.; Liu, R.; Lafrenz, T. J.; Ley, K. L.; Smotkin, E. S.; Reddington, E.; Sapienza, A.; Chan, B. C.; Malouk, T. E.; Sarangapani, S. *J. Phys. Chem. B* **1998**, *102*, 9997.

Figure 6. Correlation of EXAFS (heavy and light dotted lines), AXAFS (dashed), and $\Delta\mu$ (heavy and light solid lines) data for anode (I) in H$_2$ as a function of current. The coordination numbers $N_{PtPt} - 6$, N_{Pt-Ru}, and N_{PtO} obtained from Table 1, (AXAFS × 10^4 − 200)/40 with AXAFS obtained from Table 1, and the $\Delta\mu$ amplitudes for [OH/PtPt]/4 and OH/PtRu obtained from Figure 3 are indicated as labeled with the EXAFS (AXAFS) data relative to the left axis and $\Delta\mu$ relative to the right axis.
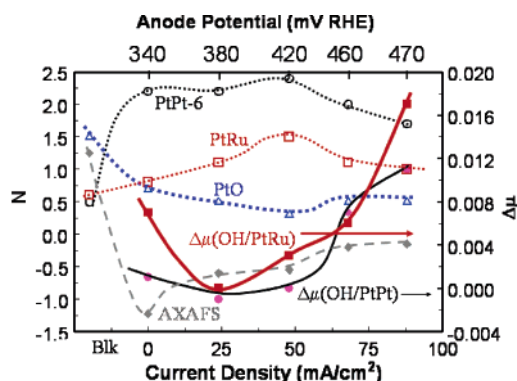
Figure 7. Correlation of EXAFS (heavy and light dotted lines), AXAFS (dashed), and $\Delta\mu$ (heavy and light solid lines) data for anode (II) in methanol as a function of current. The coordination numbers $N_{PtPt} - 6$, N_{Pt-Ru}, and N_{PtO} obtained from Table 2, (AXAFS × 10^4 − 200)/40 with AXAFS obtained from Table 2, and the $\Delta\mu$ amplitudes for OH/PtPt and OH/PtRu obtained from Figure 4 are indicated as labeled with the EXAFS (AXAFS) data relative to the left axis and $\Delta\mu$ relative to the right axis. The numbers at the top indicate the anode potential (V RHE) estimated from Figure 8 as described in the text.

not only how these data complement each other, but reveals more specifically the nature of the reduction of the electrode with current. Figures 6 and 7 compare the EXAFS coordination numbers, N, for Pt−Pt (actually $N_{PtPt} - 6$ to fit on the scale), Pt−Ru, and Pt−O along with the amplitude of the AXAFS contribution. Here the AXAFS amplitude is plotted as (AXAFS × 10^4 − 200)/40 to highlight the change with potential and to fit the AXAFS magnitude on the N scale. Finally, the amplitude of the peak around 3 eV in the $\Delta\mu$ spectrum, $\Delta\mu$(OH/PtPt), reflecting the relative OH coverage in an atop position on a Pt atom with only Pt neighbors, and the amplitude of the peak around −1 eV, $\Delta\mu$(OH/PtRu), reflecting the relative OH coverage in an atop position on a Pt atom with also Ru neighbor atoms, are also plotted.

Figure 6 shows that the blank PtRu electrode is highly oxidized, with the $N_{Pt-O,C}$ contribution almost 4 times larger, and the $\Delta\mu$(OH/PtPt) 10 times larger, than that for the in situ electrode at all currents. Upon insertion into the cell in hydrogen, $N_{Pt-O,C}$ and $\Delta\mu$(OH/PtPt) decrease from the blank sample very quickly and then slowly decrease further with current. The intensity of the $N_{Pt-O,C}$ of 0.3 at high currents probably reflects mostly Pt−C coordination resulting from the Pt atoms near the C support, since at these high currents the Pt clusters should be

mostly reduced. Proceeding in nearly reverse fashion to the Pt−O coordination as expected is the Pt−Pt coordination, small for the blank sample and increasing substantially already at 0 current and then leveling off. N_{Pt-Ru} also increases with current but at a much slower rate between blank and 20 mA/cm² than for N_{Pt-Pt}, but then increases faster than N_{Pt-Pt} beyond 30 mA/cm². A small rise occurring in N_{Pt-Pt} around 30 mA/cm² is matched by a larger rise in N_{Pt-Ru} at this same current. At this same 30 mA/cm² current, a sharp drop in $\Delta\mu$(OH/PtRu) appears.

The EXAFS results of anode II in methanol (Figure 7) are comparable to the results in Figure 6 for anode I in hydrogen. Below 30 mA/cm², the trends in the data are remarkably consistent with those in hydrogen; a strong decrease in $N_{Pt-O,C}$ is seen along with an increase in N_{Pt-Pt} indicating reduction of the PtRu electrode. Further reduction of the electrode around 30 mA/cm² is observed in the methanol data, similar to that in hydrogen, as revealed by N_{Pt-Pt}, N_{Pt-Ru}, and now also seen in $N_{Pt-O,C}$.

All of these results indicate that the hydrous RuO(H)$_n$ islands on the Pt surface, or at least the Pt atoms near the Ru islands, are more difficult to reduce than those Pt far removed from the Ru islands (i.e., the number and nature of the Pt neighbors (Pt or Ru) affect the reduction of the Pt). This is expected because Ru is much more oxophilic compared with Pt. Thus, the $\Delta\mu$-(OH/PtRu) in H$_2$ shows two reduction thresholds, one corresponding to the Pt surface and the other to the PtRu boundary regions on the surface. The latter reduction is probably occurring in concert with some reduction of the hydrous RuO(H) islands on the PtRu surface.

The observed reduction of the H anode with increasing current might at first appear as a contradiction, since oxidation should occur with increasing anode potential; however, the increase of the H anode potential with current is generally negligible. We believe that the more oxophilic Ru (and in particular some more reactive edge and/or corner Ru sites) can activate water all the way down to 0 V RHE. We have shown previously that Co atoms at the surface of PtCo alloy clusters remain oxidized to below 0.1 V RHE,[42] and CV curves for Ru suggest the same.[55] However, as the rate of H electrosorption and oxidation rate increases (with current) in the fuel cell, this weakly bound O is removed via reaction with the adsorbing/desorbing H. Therefore the O[H] coverage on the Ru, and possibly even on the Pt sites next to the Ru interface, increases as the current decreases.

Charging Effects and Estimation of the Electrode Potential. The AXAFS magnitude in H$_2$ (Figure 6) tracks with the Pt−O coordination between blank and 20 mA/cm², dropping sharply from the value for the blank sample to 0 current. This occurs because the O atoms strongly polarize the Pt potential via the field effect thus increasing the AXAFS amplitude. The strong effect of O on the Pt potential, and consequent enhancement of the AXAFS amplitude, has been discussed extensively before.[56−58] Above 30 mA/cm², the AXAFS amplitude stays relatively constant but does increase slightly coincident with
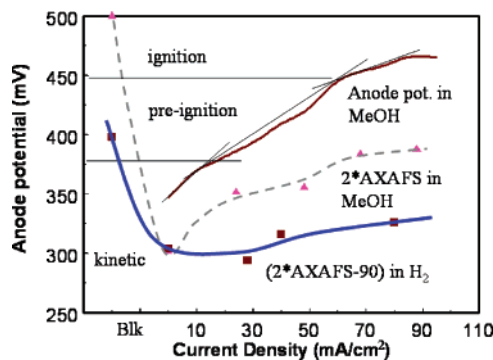
Figure 8. Plot of the anode (II) potential in methanol obtained as described in the text along with the AXAFS amplitude (obtained from Tables 1 and 2 but scaled and shifted as indicated to place them on a similar scale) for anodes in H$_2$ and methanol. The kinetic, preignition, and ignition regions are indicated as suggested by the estimated tangential slopes.

changes seen in N_{Pt-Ru} and even N_{Pt-Pt}. As mentioned above oxygen bonded to Pt increases the AXAFS intensity, but now a reduction of the Ru or Pt near the RuO(H) islands appears also to increase the Pt AXAFS. The increase here can now be explained by a small polarization of the anode to higher potential with current. Such a potential increase has been shown to increase the AXAFS,[23] and a 0.01−0.03 V increase can easily cause the small increases visible in Figure 6. The AXAFS amplitude as a function of current in methanol (Figure 7) follows a path somewhat similar to that in hydrogen; initial strong decrease from the blank case, due to the reduction of the incipient oxides, but then significantly increasing above 0 mA/cm². However, the anode potential in methanol generally increases much faster and over a much larger range as we will see below. This can explain the larger increase in the AXAFS in methanol.

One disadvantage of conventional fuel cell measurements is a missing reference electrode like, e.g., in cyclic voltammetry (CV), so that only the anode−cathode potential difference, $\Delta V = V_a - V_c$ is measured as a function of current. However, one can estimate the anode potential in methanol by taking the difference, $\delta V = \Delta V(\text{methanol}) - \Delta V(\text{hydrogen}) = V_a(\text{methanol}) - V_a(\text{hydrogen})$, where it is assumed that the potential of the cathode or oxygen electrode cancels out since it is constructed similarly for both cases. Methanol crossover to the cathode is well-known in DMFCs, and this can alter the cathode; therefore this oxygen electrode cancellation may not be complete, but we assume here that this effect will be small; at most it will shift the estimated potentials a bit. Further, since it is known that the hydrogen anode only varies between 0 and 0.03 V with current,[59] the δV above is a reasonable approximation to the anode potential in methanol. This plot with current is given in Figure 8.

If indeed the increase in the AXAFS occurs as a result of polarization of the electrode as assumed above, then the AXAFS in methanol should track with the anode potential. This can be seen in Figure 8. The remarkable correlation of the AXAFS amplitude with the estimated anode potential does indeed verify this interpretation for the AXAFS variation, namely, due to the polarization of the anode. Note the much smaller increase in

(55) Schmidt, T. J.; Paulus, U. A.; Gasteiger, H. A.; Alonso-Vante, N.; Behm, R. J. *J. Electrochem. Soc.* **2000**, *147*, 2620.

(56) Ramaker, D. E.; Mojet, B. L.; Koningsberger, D. C.; O'Grady, W. E. *J. Phys.: Condensed Matter* **1998**, *10*, 8753.

(57) Ramaker, D. E.; de Graaf, J.; van Veen, J. A. R.; Koningsberger, D. C. *J. Catal.* **2001**, *203*, 7.

(58) Ramaker, D. E.; van Dorssen, G. E.; Mojet, B. L.; Koningsberger, D. C. *Top. Catal.* **2000**, *10*, 157.

(59) Mukerjee, S.; Urian, R. C.; Lee, S. J.; Ticianelli, E. A.; McBreen, J. *J. Electrochem. Soc.* **2004**, *151*, A1094; Mukerjee, S.; Urian, R. C. *Electrochima Acta* **2002**, *47*, 3219; Urian, R. C. Ph.D. Thesis, Northeastern University, Boston, MA, 2003.
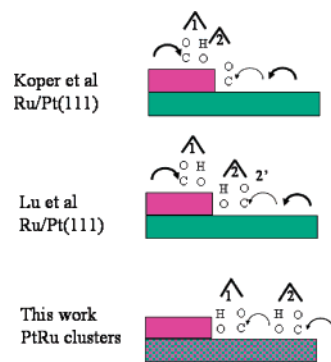
the AXAFS for H_2, consistent with the much smaller change in anode potential with current (<0.03 V).

RuO(H)$_n$ and Its Role in Bifunctionality versus Ligand Effects. Figure 8 shows that between 30 and 90 mA/cm^2 the anode polarization potential varies in the range of $370-470$ mV. These potentials are apparently sufficiently large to allow activation of water (i.e., adsorption of OH) on PtRu. This adsorption of OH is directly evident from the increase in OH coverage above 30 mA/cm^2 in methanol as revealed in the $\Delta\mu$'s of either Figures 5 or 7. Of course this adsorption of OH also accounts for the CO stripping peak seen in typical CV curves in this potential region[8,60-62] consistent with the Langmuir–Hinshelwood type surface reaction between CO$_{ad}$ and OH$_{ad}$.

However, two thresholds for OH adsorption on Pt are revealed in the $\Delta\mu$ data in methanol, one at about 30 mA/cm^2 in $\Delta\mu$-(OH/PtRu) and one at 60 mA/cm^2 in $\Delta\mu$(OH/PtPt). On Pt(111) in CO with HClO$_4$ as electrolyte, two similar thresholds at 0.4 and > 0.6 V for OH formation and CO oxidation have been called the "preignition" and "ignition" regions by Markovic et al.[63] These were attributed to OH formation at defect sites and on the (111) faces, respectively. In the results presented here these thresholds for OH formation are occurring at still lower anode potentials, since these threshold currents in methanol correspond to the anode potential of about 370 and 450 mV (see horizontal lines in Figure 8). Two well-resolved current peaks at 0.55 and 0.67 V RHE in CO stripping from small Ru islands on Pt(111) have also been reported. Finally, FTIR and SFG data show two distinctive atop CO species which have been attributed to CO chemisorbed on the Ru sites and those on the Pt sites.

The similar "preignition" region visible in Figures 5 and 7 is believed to result from OH production on or near the hydrous RuO(H)$_n$ with CO oxidation via the bifunctional mechanism. This is indicated here because the preignition region occurs only in $\Delta\mu$(OH/PtRu), i.e., on the Pt but near the RuO(H)$_n$ islands. In contrast, the ignition region is due to OH formation directly on the PtRu alloy but removed from the RuO(H)$_n$ islands, with threshold around 0.45 V. This is shifted down from that in pure Pt/C at >0.6 V due to an electronic "ligand" effect resulting from the alloying with Ru.[13-16] Thus both CO oxidation mechanisms are suggested to play a role here. The near overlap of the preignition OH threshold with reduction of the hydrous RuO(H) islands, as exhibited in Figure 7, may not be coincidental, since more metallic Ru sites (not RuO(H)$_n$ sites) may be required for the adsorption of OH on or near the Ru.

Figure 5b compares a plot of the CO(O) coverage versus the OH/PtPt and OH/PtRu coverage as obtained from the $\Delta\mu$ XANES results. These data show the strong reduction in CO coverage around 60 mA/cm^2, right at the ignition threshold for the OH formation on PtRu as expected. The decrease in apparent CO(O) coverage below 22 mA/cm^2 is attributed not to oxidation of CO but to desorption of O$_{br}$/Pt, as the O$_{br}$/Pt feature at 7 eV overlaps with the CO signature (see Figure 4) and contributes to the CO(O) intensity. We expect a significant reduction of the O$_{br}$/Pt feature along with the OH atop peaks with increase

(60) Morimoto, Y.; Yeager, E. *J. Electroanal. Chem.* **1998**, *444*, 95.
(61) Massong, H.; Wang, H.; Samjeské, H.; Baltruschat *Electrochimica Acta* **2000**, *46*, 701.
(62) Russell, A. E.; Maniguet, S.; Mathew, R. J.; Yao, J.; Robers, M. A.; Thompsett, D. *J. Power Sources* **2001**, *96*, 226.
(63) Marković, N. M.; Lucas, C. A.; Rodes, A.; Stamenković, V.; Ross, P. N. *Surf. Sci.* **2002**, *499*, L149.

Figure 9. Schematic illustration of the different mechanisms proposed to account for the two voltametric peaks seen in CO stripping from Ru(O)$_n$ islands (shaded dark) deposited on Pt(111) (shaded light) by Koper and co-workers[64,65] and by Lu et al.[16] In contrast are the mechanisms proposed in this work for the two thresholds evident in methanol oxidation (allowed by CO stripping) on PtRu (checkered). Numbers under the hats indicate which peak the mechanism is believed to contribute (1 = prepeak and 2 = normal), and the curved arrows indicate CO hopping (fast by the thick arrows and slower by the thin).

in potential from 0 to 22 mA/cm^2. The solid line in Figure 5b separates the expected CO and O$_{br}$ components in this region. The increase of CO coverage with current between 25 and 60 mA/cm^2 suggests that the CO coverage increases with current throughout the preignition region, consistent with previously reported results.[43] Figure 5 shows that the CO coverage is about half of the maximum coverage already at low potential (i.e., in the H region). This is in contrast to that found by Waszczuk et al.,[43] who find that the initial coverage is near zero. However, these results are not really inconsistent since methanol adsorption is apparently a slow process in the H region, and the results of Waszczuk et al. were scanned at 50 mV/s, and our results are obtained after equilibrium is reached. Apparently, only above the ignition threshold does OH formation take over with methanol adsorption becoming the RDS, consistent with previous kinetic studies.

Finally, Figure 8 shows that the anode potential increases much faster in the preignition (bifunctional) region than in the ignition region. This is expected, since as the results in Figure 5b show, the OH is in excess well above the ignition threshold so that the potential does not need to increase appreciably to create more OH. It can be seen in Figure 8 that both the anode potential and AXAFS in methanol increase very fast in the "kinetic" region due to the kinetic overpotential, but this is not seen in the AXAFS for the electrode in H_2 as expected, since the kinetic over potential for H adsorption is small.

Mechanism for Electrooxidation of CO from Ru/Pt(111) versus PtRu Clusters. The mechanisms for the electrooxidation of CO from *model* catalysts such as small Ru clusters deposited on Pt(111) have been extensively studied and discussed in the literature. Two voltametric stripping peaks for CO oxidation (a prepeak and a normal peak when scanned at around 50 mV/s) are also seen for these model catalysts, but the mechanisms for these separate peaks, as summarized in Figure 9, are very different from what we propose here. Koper and co-workers[64,65] attribute the prepeak to CO oxidation of CO/Ru (mechanism 1) and the normal peak to CO stripping of CO/Pt via the normal

(64) Koper, M. T. M.; Lukkien, J.; Jansen, A. P. J.; van Santen, R. A. *J. Phys. Chem. B* **1999**, *103*, 5522.
(65) Koper, M. T. M.; Lebedeva, N. P.; Hemse, C. G. M. *Faraday Discuss.* **2002**, *121*, 301.

bifunctional mechanism (i.e., via reaction with OH/Ru near the edge of the Ru islands indicated as mechanism 2). Koper and co-workers assume fast hopping of the CO on the Pt(111) surface but show via theoretical calculations that a slow hop of the CO to the PtRu edge site is required to account for the separation between the two peaks. On the other hand Lu et al.[16] find two separate reaction rates in the second voltametric peak using double-potential step chronoamperometry. They therefore propose that the first reaction rate arises from stripping of the CO near the Ru island edge as shown by process 2 in Figure 9 and the second rate arises from diffusion of the CO from further way to the island edge (mechanism 2′).

For direct comparison we show the two processes which we propose for the preignition and ignition regions, respectively, in this work. The very existence of OH/PtRu when large amounts of CO are still present indicates that much of the CO is unable to hop to the edge of the RuO(H)$_n$ islands. We propose that both CO/RuO(H)$_n$ and CO/PtRu stripping appear in the preignition region (the former not observed in this work) and that the regular ignition region arises from direct OH adsorption on the Pt as indicated above. Figure 5b shows that the bulk of the CO stripping arises only when OH/Pt is also visible.

The differences between the model catalyst and our PtRu alloy particles are primarily responsible for these different mechanisms. Certainly the CO is not as mobile on the PtRu particles as on Pt(111), because the CO binding energies will be higher at corners and edges of the PtRu particles. Therefore OH formation directly on the Pt is required to remove more of the CO, but this threshold is shifted significantly down in potential (i.e., a Ru ligand or electronic effect on the Pt) because of the PtRu alloy formation, which does not occur significantly in the Ru/Pt(111) model catalysts. Thus, the large ligand effect is expected only when significant alloying occurs such as in these PtRu alloy particles. The ligand effect is believed to arise primarily from increased activation with water to form OH at lower potentials rather than weakening of the CO−Pt bond.

Conclusions

A special in situ fuel cell for X-ray absorption spectroscopy was developed and allowed for the Pt−Ru electrode structure and adsorbate coverage to be followed as a function of the current in either hydrogen or vaporized 1 M methanol solution at elevated temperatures. Variations in both the coverage of O[H] and CO ($\Delta\mu$ technique) as well as in the geometric (EXAFS) and electronic (atomic XAFS) structure of the anode catalyst were monitored as a function of the current. The results obtained with the $\Delta\mu$ technique, EXAFS, and AXAFS were found to correlate with each other.

From these data we draw the following conclusions: (1) The strong correlations observed indicate that consistent structural, electronic, and adsorbate coverage data can be obtained even on rather large PtRu clusters (where the dispersion is as small as 0.4). Even for these large clusters the $\Delta\mu$ technique is able to collect *operando* information about surface reactions as a function of the current in a PEM fuel cell. (2) The obtained data and correlations allow the direct observation of the preignition and ignition regions for OH formation and CO oxidation during the methanol fuel cell operation. These two regions are attributed to both the bifunctional mechanism involving OH formation on or near the RuO(H)$_n$ islands and to the direct formation of OH on PtRu shifted down from pure Pt by nearly 0.1 V by an electronic ligand effect. (3) The two CO stripping mechanisms found in this work are contrasted with that proposed previously on Ru/Pt(111) model catalysts.

Supporting Information Available: Several additional figures and results providing details on the EXAFS and XANES analysis. This material is available free of charge via the Internet at http://pubs.acs.org.

JA050139F